Volume 14
Number 12
21 June 2024
Pages 3267–3570

Catalysis Science & Technology

rsc.li/catalysis

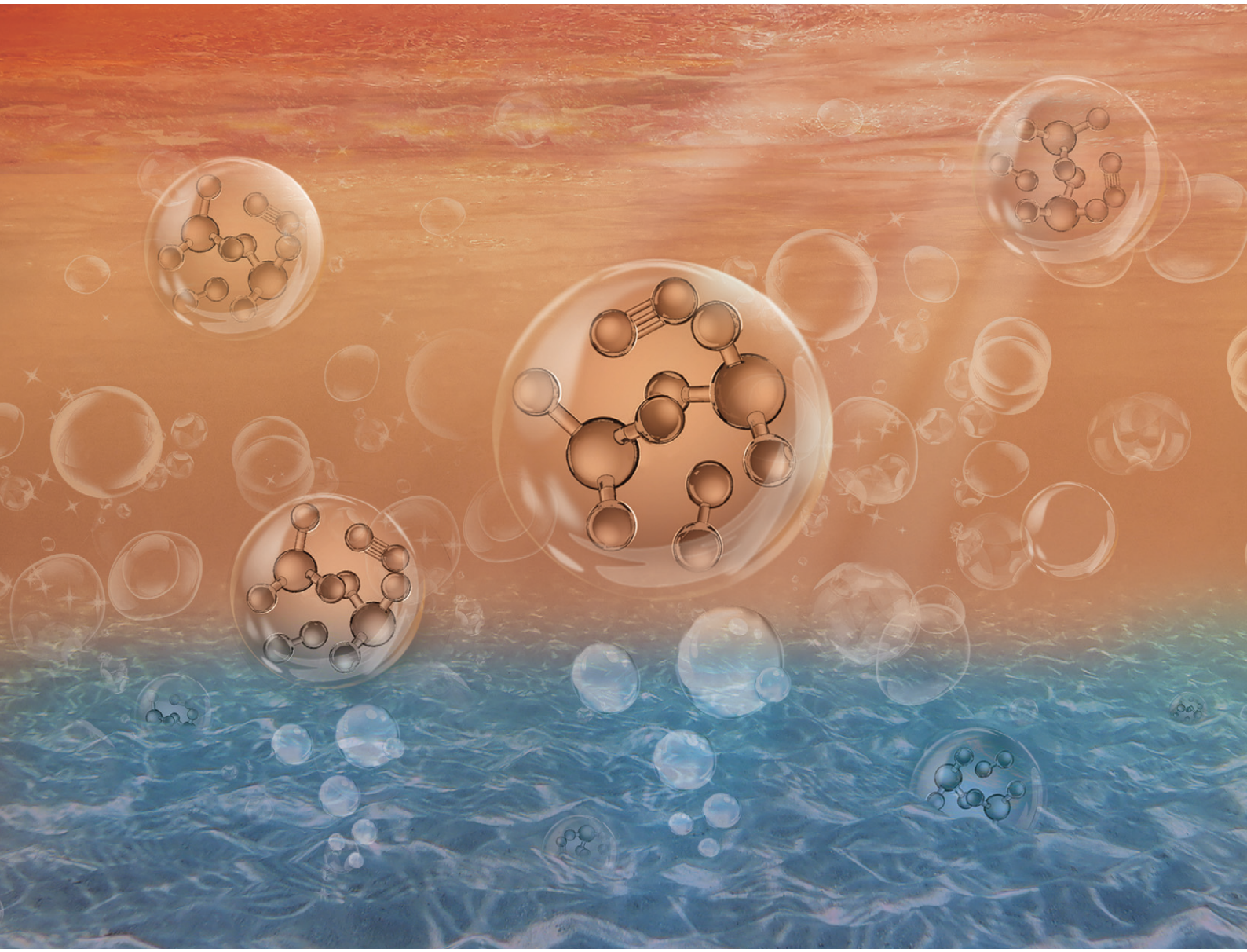

ISSN 2044-4761

ROYAL SOCIETY OF CHEMISTRY

PAPER

Xian Meng, Xiaofei Guan *et al.*

Molten multi-phase catalytic system comprising Li–Zn alloy and LiCl–KCl salt for nitrogen fixation and ammonia synthesis at ambient pressure

Catalysis Science & Technology

ROYAL SOCIETY OF CHEMISTRY

PAPER

View Article Online
View Journal | View Issue

Check for updates

Cite this: *Catal. Sci. Technol.*, 2024, 14, 3320

Molten multi-phase catalytic system comprising Li–Zn alloy and LiCl–KCl salt for nitrogen fixation and ammonia synthesis at ambient pressure†

Xian Meng,‡ Jian Liu, ‡ Zujian Tang, Bingxu Xi, Pu Yan, Xingran Wang, Kecheng Cao, Bo Yang * and Xiaofei Guan *

Received 14th February 2024,
Accepted 23rd March 2024

DOI: 10.1039/d4cy00202d

rsc.li/catalysis

Ammonia (NH_3) is one of the most important synthetic inorganic commodities. The current industrial NH_3 production is dominated by the Haber–Bosch process with high energy cost and CO_2 emission as well as the need for large-scale centralized operation. Liquid metals and molten salts have recently emerged as promising catalytic materials for NH_3 synthesis. Herein, we present a molten system comprising Li–Zn alloy and eutectic LiCl–KCl salt for effective NH_3 synthesis at 400 °C and 1 bar. The 70 mol% Li–Zn liquid alloy activates N_2 dissociation more easily than the pure liquid Zn and the 60 mol% Li–Sn liquid alloy. Effective N_2 fixation by the liquid Li–Zn alloy is followed by the hydrogenation of Li_3N dissolved in the molten salt above. For the first time, this work reports a volcano-type relationship between the Li_3N concentration in the molten salt and the NH_3 synthesis rate when feeding H_2 to the molten salt. *Ab initio* molecular dynamics simulations suggest that, within this system, both N_2 cleavage and Li_3N hydrogenation are quite reactive. Through combined experiments and simulations, this work unravels the molecular mechanisms of nitrogen fixation and ammonia synthesis in the liquid alloy–salt catalytic system, and also demonstrates effective strategies for improving the ammonia synthesis rate. Such a hybrid molten catalytic system offers a promising solution for distributed NH_3 production with low energy cost and CO_2 emission.

1. Introduction

The ammonia (NH_3) industry plays a significant role in the world economy.[1] More than 80% of synthetic NH_3 is used as a raw material for the production of agricultural fertilizer,[2] which is a key to food security. Small fractions of NH_3 are used as a refrigerant, cleaning agent, and pharmaceutical feedstock.[3] In addition, NH_3 has recently re-emerged as an important and carbon-free energy carrier due to its advantages including high energy density (3 kW h kg^{-1}), high hydrogen content (~18 wt%), facile storage and transportation, and the infrastructure maturity.[4,5]

Currently, the industrial production of NH_3 still relies on the Haber–Bosch process, a technology invented over a century ago.[6] Hydrocarbon steam reforming of high emissions is often utilized to provide H_2, although renewable H_2 from water electrolysis is under heavy investigation as a new supply.[1,7,8] The Haber–Bosch process combines H_2 with N_2 separated from air in a high-temperature (400–600 °C) and high-pressure (100–300 bar) reactor containing iron-based catalysts to produce NH_3. The reaction is expressed as

$$N_2 + 3H_2 \rightarrow 2NH_3 \quad (1)$$

Nevertheless, the conventional Haber–Bosch process suffers from various drawbacks. For example, it consumes 1–2% of the global energy supply, and it is responsible for approximately 1.2% of global CO_2 emissions.[9,10] Moreover, the energy cost of transporting fertilizer to remote areas needs to be considered because of the centralization of large-scale Haber–Bosch plants. To reach global carbon neutrality and align with the United Nations' Sustainable Development Goals,[11] there is an urgent need to develop novel, energy-efficient, and environmentally friendly technologies for distributed NH_3 synthesis.

Extensive studies have been conducted over the past decades with the goal of producing NH_3 under milder conditions. Compared with first-generation iron-based catalysts, ruthenium-based catalysts synthesize NH_3 at lower temperatures (300–450 °C) and pressures (40–150 bar), but their applications are constrained by the high cost and severe H_2 poisoning.[5,12–14] To improve the catalytic performance of transition metals, it is important to modify the nitrogen

School of Physical Science and Technology, ShanghaiTech University, 393 Huaxia Middle Road, Shanghai, 201210, China. E-mail: yangbo1@shanghaitech.edu.cn, guanxf@shanghaitech.edu.cn

† Electronic supplementary information (ESI) available. See DOI: https://doi.org/10.1039/d4cy00202d

‡ These authors contributed equally.

adsorption energy or even circumvent the scaling relation exerted on them.[15–24] For example, Wang *et al.* employed LiH as the second active center for hydrogenation to intervene in TM-mediated catalysis and achieved high catalytic activities at only 150–350 °C and 1 bar.[16] Peng *et al.* have reported a RuCo dual single-atom active catalyst to decouple the sites for N_2 activation from those for the desorption of N-containing intermediate species, and realized a high synthesis rate of NH_3 at merely 200 °C and 10 bar.[19] In addition, the ternary intermetallic electride LaCoSi and the related dual-site mechanism studies have been reported for effective ammonia synthesis with N_2 dissociation on the Co site and N hydrogenation on the La site, circumventing the scaling relation.[25–28]

The search for non-transition metal catalysts with high activity, stability, and cost effectiveness represents another important research direction. Kawamura and Taniguchi have reported a route using sodium (Na) melt as an effective catalyst for NH_3 synthesis from N_2 and H_2 at 500–590 °C under atmospheric pressure.[29] The function of the liquid Na was to ionize N_2 and dissolve nitrogen.[30] In addition, Li has been reported to spontaneously split the triple bond in N_2 to form Li_3N under ambient conditions.[31] Li_3N can be protonated by H_2O to form NH_3 and LiOH; the LiOH product can be electrolyzed to regenerate Li, closing the loop.[32] However, the step of LiOH electrolysis remains a challenge mainly due to the consumption of Li by LiOH.[33,34] Solid Li-based alloys have also gained significant research attention for thermocatalytic NH_3 synthesis.[35,36] For example, Yamaguchi *et al.* reported NH_3 synthesis from N_2 and H_2 using a solid Li–Sn alloy below 400 °C under ambient pressure.[37] However, the solid Li–Sn pseudo-catalyst suffered from performance degradation after the first cycle. Meanwhile, the hydrogenation of the intermediates (*e.g.*, $LiNH_2$, Li_2NH) was limited by both thermodynamics and kinetics.[38] The reaction kinetics between Li_2NH and H_2 for NH_3 synthesis might be improved by the addition of Li_2O as a scaffold material.[39] Recently, Tang *et al.* reported an innovative Li-based loop for NH_3 synthesis in a liquid catalytic system comprising a Li–Sn alloy and LiCl–KCl salt.[40] The materials used were earth abundant and did not need complicated preparation. The liquid alloy and molten salt self-segregated by density into two distinct layers due to their immiscibility.[33,41] The Li-based loop consisted of three simultaneous steps: (i) N_2 fixation by Li in the liquid alloy to produce Li_3N, (ii) the hydrogenation of Li_3N dissolved in the molten salt to form NH_3 and LiH, and (iii) LiH decomposition to regenerate Li. The liquid catalytic system took advantage of the floating and dissolution of Li_3N into the molten salt and circumvented the scaling relation exerted on Li, leading to effective NH_3 synthesis. In place of alkali metals, alkaline earth metals might also be candidate materials for fixing N_2 due to their high reactivity and low cost.[32,40,42] However, the mechanisms for nitrogen fixation and ammonia synthesis remained elusive, and the operation temperature of the liquid alloy–salt catalytic systems reported was relatively high (*e.g.*, 510 °C for the system with a Li–Sn liquid alloy and LiCl–KCl molten salt). For a fixed pressure, lowering the operating temperature is critically important for increasing the equilibrium molar fraction of the NH_3 product based on the thermodynamic analysis.[40,43] The goal of unlocking the full potential of the liquid alloy–salt catalytic systems for NH_3 synthesis motivates the investigations, particularly unveiling the mechanisms of NH_3 formation and release.

It is necessary to identify the ideal materials for the liquid alloy–salt catalytic systems to achieve high performance. Based on the previous work,[40] several criteria are proposed here, including: (i) spontaneous reaction of N_2 with the reactive metal to form a metal nitride when the alloy (or metal) is exposed to N_2, (ii) facile transport (*e.g.*, flotation, diffusion) of the metal nitride from the alloy (or metal) to the salt, (iii) easy dissolution and ionization of the metal nitride in the salt, (iv) spontaneous reaction between the nitride ion and the proton source to produce NH_3; a metal hydride or salt is also formed depending on the type of proton source, (v) the easy release or collection of NH_3 from the catalytic system, and (vi) effective conversion of the metal hydride or salt formed in (iv) back to the reactive metal. According to the phase diagram,[44] the Li–Zn alloy of appropriate composition remains liquid at relatively low temperatures (Fig. S1a†). In addition, Li–Zn has a greater Li activity than Li–Sn for a fixed Li content,[45] indicating a greater capacity for N_2 fixation. Based on these properties, the liquid Li–Zn is investigated as a promising alloy candidate in the liquid catalytic system for operating at lower temperatures.

Fig. 1a shows a schematic of the liquid alloy–salt catalytic system. N_2 and H_2 are fed through the bubbling tubes to the

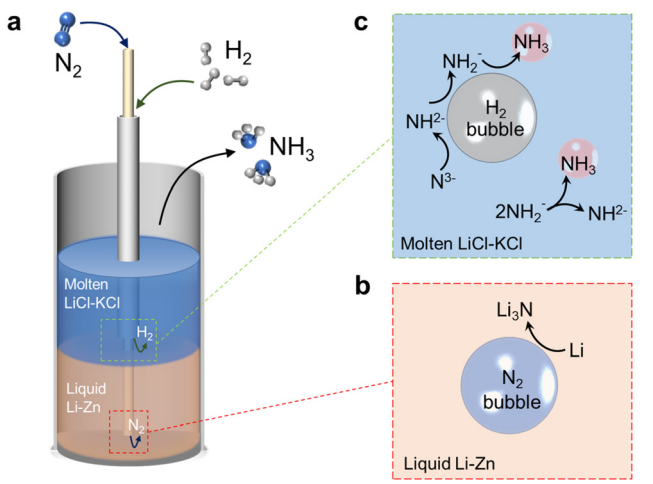

Fig. 1 (a) Schematic illustration of the liquid catalytic system comprising the Li–Zn alloy and LiCl–KCl eutectic salt for NH_3 synthesis from N_2 and H_2 inside an alumina bubble-column reactor. (b) N_2 fixation by Li in the liquid Li–Zn alloy to form Li_3N at the N_2 bubble/alloy interface. (c) The N^{3-} ions in the molten salt react with H_2 to produce NH^{2-}, NH_2^- and NH_3, successively, at the H_2 bubble/salt interface. Additionally, the bimolecular decomposition of NH_2^- for producing NH_3 and NH^{2-} is also shown.

bottoms of the Li–Zn liquid alloy and LiCl–KCl molten salt, respectively. N_2 is fixed by Li in the Li–Zn liquid alloy to form Li_3N (reaction (2) and Fig. 1b). Driven by the buoyancy and also the rising bubbles, Li_3N floats up to the molten salt and dissolves into Li^+ and N^{3-} because the highly ionic molten salt has enough attraction to break down the Li_3N compound (reaction (3)).[46,47] The N^{3-} ions react with H_2 to form NH_3 and H^- (reaction (4) and Fig. 1c). Reaction (4) occurs stepwise *via* the formation of the imide ion (NH^{2-}) and the amide ion (NH_2^-), as expressed by reactions (4a)–(4c).[48] In the presence of Zn, a small portion of the LiH product (a combination of Li^+ and H^-) might decompose to regenerate Li that alloys with Zn at the alloy/salt interface (reaction (5)).[40,49,50] In addition, NH_3 can also be produced by bimolecular decomposition of NH_2^- (reaction (6) and Fig. 1c).[48] The standard molar Gibbs free energy change of the relevant reactions in the Li–N–H system are shown in Fig. S1b.† We systematically study the roles of multiple variables in nitrogen fixation and ammonia synthesis, and gain a deeper understanding of the process through combined experiments and modeling. The catalytic system integrates the functions of the Li–Zn liquid alloy and the LiCl–KCl molten salt, and is demonstrated for effective NH_3 synthesis at relatively low temperatures and ambient pressure.

$$N_2 + 6Li_{(Zn)} \rightarrow 2Li_3N \quad (2)$$

$$Li_3N \rightarrow 3Li^+ + N^{3-} \quad (3)$$

$$N^{3-} + 3H_2 \rightarrow NH_3 + 3H^- \quad (4)$$

$$N^{3-} + H_2 \rightarrow NH^{2-} + H^- \quad (4a)$$

$$NH^{2-} + H_2 \rightarrow NH_2^- + H^- \quad (4b)$$

$$NH_2^- + H_2 \rightarrow NH_3 + H^- \quad (4c)$$

$$2LiH \rightarrow 2Li_{(Zn)} + H_2 \quad (5)$$

$$2NH_2^- \rightarrow NH^{2-} + NH_3 \quad (6)$$

2. Experimental section

2.1. Pretreatment of the Li–Zn mixture and the LiCl–KCl eutectic salt

The volume expansion caused by the Li–Zn alloying is relatively small.[51] However, considering the large difference in the melting point and the density between Li and Zn, solid Li and Zn were pretreated to prepare the Li–Zn mixture, which would make the complete alloying easier in the subsequent high-temperature experiments. The desired amounts of Li strips and Zn granules were mixed in a small alumina crucible (OD: 14 mm, ID: 12 mm, height: 44 mm) that was placed in a bigger alumina container (OD: 80 mm, ID: 76 mm, height: 100 mm) with an alumina cover. The system was heated at 260 °C for 2 hours on a hot plate (IKA, RCT Basic) inside an Ar-filled glovebox. The phases of the pre-treated Li–Zn mixture were determined to be LiZn and Li by X-ray diffraction (Fig. S3†).

To remove the moisture, the LiCl or KCl powders were transferred to an alumina crucible (OD: 80 mm, ID: 76 mm, height: 100 mm) in an electric furnace, and heated at 300 °C for 12 hours under vacuum, during which Ar was flowed into the system at 20 cm^3 min^{-1}. The pre-treated salt was collected and stored in the Ar-filled glovebox. LiCl and KCl were weighted with a molar ratio of 0.592 : 0.408 and fully mixed using a vortex mixer (Vortex-Genie 2, Scientific Industries, Inc.) for 10 minutes to obtain the LiCl–KCl eutectic mixture. The actual amounts of metals and salts used for different experimental conditions are shown in Table S2.†

2.2. Bubble column reactors for NH_3 synthesis

Bubble column reactors were assembled using one-end-closed alumina tubes (OD: 18 mm; ID: 13 mm; height: 400 mm) and Swagelok Ultra-Torr™ vacuum fittings, as shown in Fig. S2.† The pretreated Li–Zn mixture and LiCl–KCl eutectic mixture were transferred sequentially to the alumina tube and sealed by vacuum fittings. The assembly was done in an Ar-filled glovebox with O_2 and H_2O levels less than 10 ppm.

Inside a vertical electric furnace, the reactor fed with Ar (20 cm^3 min^{-1}) was first maintained at 300 °C for 12 hours under vacuum to remove the moisture. Afterwards, the temperature was ramped to 500 °C, maintained for 30 min, and then cooled to 400 °C under Ar atmosphere to obtain the Li–Zn liquid alloy (height: ~5 cm) and LiCl–KCl eutectic molten salt (height: ~5 cm). The density of the 70 mol% Li–Zn alloy (2.33 g cm^{-3}) is greater than that of LiCl–KCl eutectic salt (1.69 g cm^{-3}) at 400 °C,[52–54] so the alloy was below the salt. Then, pure N_2 (5 cm^3 min^{-1}) and H_2 (15 cm^3 min^{-1}) were introduced into the reactor in either a separate or mixed way. The flow rates of N_2 and H_2 were regulated using mass flow controllers (MFC; Omega Engineering Inc., Part No.: FMA5508A).

The NH_3 product in the effluent gas was absorbed by 0.05 mol L^{-1} H_2SO_4 aqueous solution (10 mL) which was replaced every two hours to determine the NH_3 synthesis rate. A colorimetric indicator method was coupled with ultraviolet visible spectroscopy (UV-Vis) for quantification of NH_3 trapped in the H_2SO_4 aqueous solution based on the NH_3 standard calibration curve.[40] An Agilent Cary 5000 UV-Vis–NIR spectrophotometer was used to obtain the relationship between the absorbance and the wavelength.

2.3. Material characterization

X-ray diffraction (XRD) with Cu Kα radiation and a θ–2θ diffraction geometry was used to determine the crystalline phases of the solidified alloy and salt (Bruker, D8 Advance, USA). The crystalline phases were identified with the International Centre for Diffraction Data (ICDD) powder diffraction file (PDF)-4+ database. The sample preparation

was carried out in an Ar-filled glovebox, and polyimide tape was used to seal the sample to prevent oxidation during the sample transfer and XRD measurement. Chemical elements on the alloy or salt surface were analyzed using X-ray photoelectron spectroscopy (XPS) with an ESCALAB™ 250Xi XPS microprobe (Thermo Fisher Scientific, USA). The NIST XPS database was used for chemical state identification.[55] All binding energies were calibrated by referencing to the C 1s peak of adventitious carbon at 284.8 eV, similar to previous reports.[56,57] The sample was prepared in an Ar-filled glovebox and then transferred to the XPS sample chamber using a portable sample transfer-bin.

Raman spectroscopy was used to characterize the samples with an Andor Shamrock SR-500i Raman system (×50 objective lens, ×600 grating, and 532 nm laser excitation). The surface morphologies and elemental distribution were studied using scanning electron microscopy (SEM) and energy dispersive X-ray spectroscopy (EDS) on a JEOL SEM IT-500HR/LA. The transmission electron microscopy (TEM) images, scanning transmission electron microscopy (STEM) images and electron energy-loss spectroscopy (EELS) results were collected using a 300 kV aberration-corrected transmission electron microscope (JEOL GrandARM-300F) equipped with a double spherical corrector with a Gatan Oneview IS camera. The sample was first ground with a pestle and mortar into powders, some of which were transferred to a copper grid and then fixed in a holder for characterization. The sample preparation was all done inside an Ar-filled glovebox.

3. Results and discussion

3.1. N_2 fixation by the Li–Zn liquid alloy

3.1.1. Characterization of the solidified alloy column after the reaction. N_2 activation and fixation is the critical step for NH_3 synthesis in the liquid alloy–salt catalytic system, considering the strong N≡N triple bond.[40] We first investigated the reaction of N_2 with the Li–Zn alloy inside a bubble column reactor as illustrated in Fig. 2a. The pre-treated 70 mol% Li–Zn mixture inside the reactor was heated to 500 °C and then cooled to operation temperature (400 °C) under Ar atmosphere to obtain the liquid alloy with a height of approximately 5 cm. Then, N_2 was introduced through an alumina bubbling tube to the liquid alloy bottom at 5 cm^3 min^{-1} for 1 hour. The reactor was subsequently cooled to room temperature and dismantled for material characterization. Fig. 2b shows the XRD patterns of the samples collected from the solidified alloy column. Sample 1 was collected from the wall close to the top of the alloy column, sample 2 was collected right from the top, whereas sample 3 was collected from the lower portion. Based on the XRD pattern for sample 1, the dominant phase was identified to be high-crystallinity α-Li_3N with preferred orientations and a small amount of the LiZn intermetallic phase.[58] No

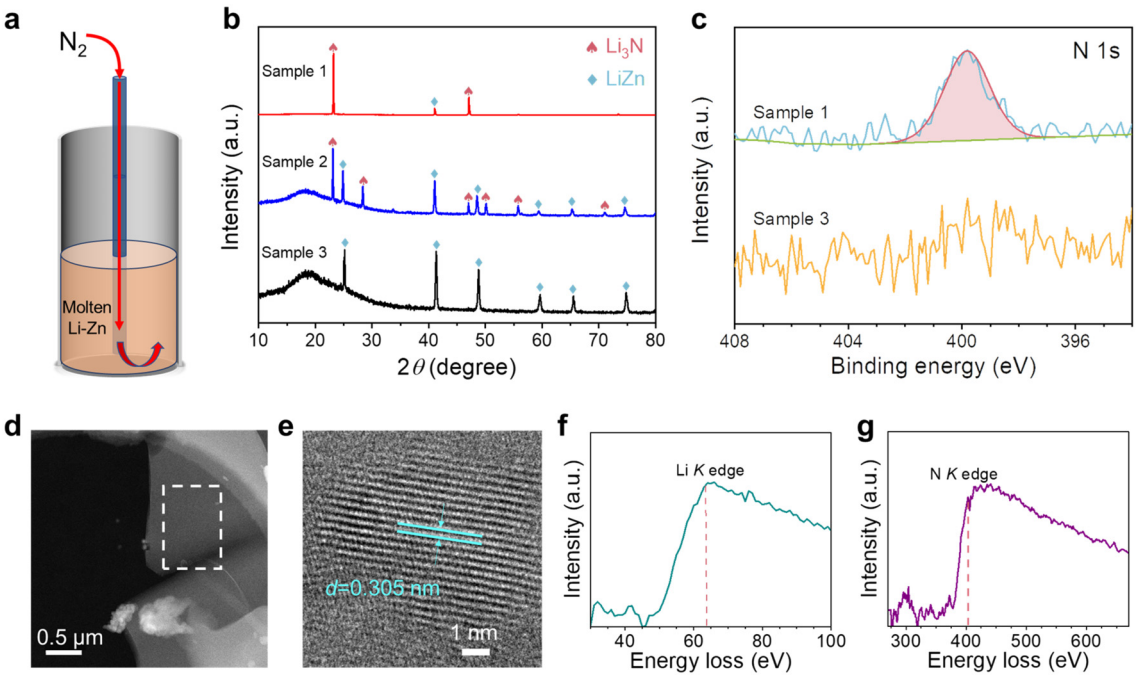

Fig. 2 (a) Schematic of the reactor containing the liquid Li–Zn alloy (height: ~5 cm) bubbled with N_2 (5 cm^3 min^{-1}). (b) XRD patterns of the three samples collected from different places of the solidified alloy column. The characteristic peaks for α-Li_3N (PDF No. 76-0820) and LiZn intermetallic (PDF No. 03-0954) were indexed. The wide signal at ~18° observed for samples 2 and 3 was attributed to the polyimide film cover. (c) High-resolution N 1s XPS results of sample 1 and sample 3. (d) STEM image for sample 1 on a copper grid. (e) High-resolution TEM image of sample 1 with the (100) interplanar spacing identified to be 0.305 nm. (f) The Li K-edge and (g) the N K-edge EELS spectra for the area enclosed by the white dashed rectangle in (d).

characteristic peaks for LiZnN or Zn_3N_2 were observed.[47,59] The presence of α-Li_3N was consistent with the XPS characterization results (Fig. 2c),[60,61] validating reaction (2). The XRD pattern for sample 2 shows the diffraction peaks for both α-Li_3N and LiZn;[58] yet, it's noted that the crystallinity seemed not as high as that in sample 1. The XRD results for sample 2 were consistent with the SEM and EDS results (Fig. S4†). The XRD pattern for sample 3 didn't show the diffraction peaks for Li_3N; the N 1s XPS result in Fig. 2c didn't exhibit the characteristic peaks either, indicating the absence of Li_3N. Li_3N (density: 1.296 g cm^{-3} at room temperature)[62] floated to the top of the liquid alloy due to the density difference and phase immiscibility.[40] It's noted that, based on the Li–Zn phase diagram[44] (Fig. S1a†), the cooling of the 70 mol% Li–Zn alloy would transform to a mixture of LiZn and Li. However, the amount of Li was below the XRD detection limit because N_2 fixation consumed some Li in the Li–Zn alloy.

To analyze the local structure and elemental composition, scanning transmission electron microscopy (STEM) and electron energy-loss spectroscopy (EELS) were used to characterize sample 1. The STEM images show the particles of sample 1 after grinding (Fig. 2d and S5†). Fig. 2e shows the lattice-resolved TEM image of sample 1, and the interplanar spacing (d) of 0.305 nm was indexed to the (100) planes of α-Li_3N. Fig. 2f and g confirmed the presence of Li and N based on their K-shell ionization edges at 63 eV and 403 eV, respectively.[63,64]

3.1.2. Kinetic parameter measurements for N_2 fixation by the Li–Zn liquid alloy. To evaluate the time dependence of N_2 fixation, we performed a series of experiments for different durations at 400 °C. To quantify the amount of nitrogen fixed by the liquid Li–Zn alloy, we proposed the use of a layer of molten LiCl–KCl (height: 5 cm; mass: 8.8 g) on top of the liquid Li–Zn to collect Li_3N through dissolution (Fig. 3a). N_2 (5 cm^3 min^{-1}) and Ar (15 cm^3 min^{-1}) were flowed into the

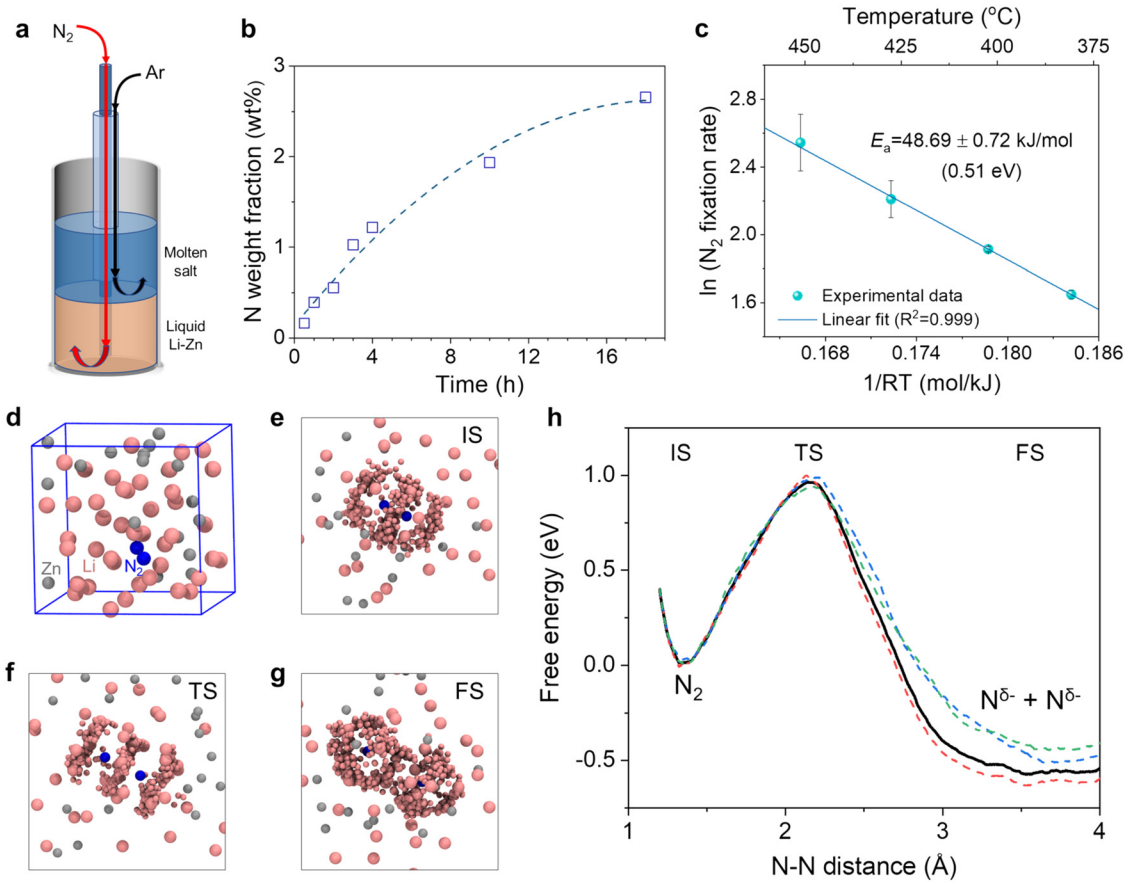

Fig. 3 Kinetics and AIMD simulation for N_2 fixation by the Li–Zn liquid alloy. (a) Schematic diagram of the reactor containing 70 mol% Li–Zn alloy (height: 5 cm) in the bottom bubbled with N_2 (5 cm^3 min^{-1}) and the eutectic LiCl–KCl molten salt (height: 5 cm) on the top bubbled with Ar (15 cm^3 min^{-1}). (b) Dependence of the nitrogen weight fraction in the salt on the reaction time. The dashed line served as a guide for the eyes. (c) Arrhenius plot for the N_2 fixation rate in the temperature range of 380–450 °C. (d) Snapshot of the model system after a pre-relax simulation for 5 ps. The cubic box represents the periodic unit cell of the infinite bulk system. Color code: pink, Li; gray, Zn; blue, N. (e–g) The local environments of the initial, transition, and final states (IS, TS, and FS) during N_2 cleavage, respectively. The statistical distribution of Li and Zn near the two nitrogen atoms was illustrated by superimposed snapshots with smaller spheres. (h) The free energy profile as a function of the N–N distance during the N_2 cleavage process, as denoted by the black bold line. The work profiles of 3 slow-growth trajectories are also shown, as denoted by the dashed lines in color.

liquid alloy and the molten salt, respectively. At the end of each experiment, Ar bubbling was kept for an extra period (30 min) to homogenize the distribution of Li_3N. Afterwards, the reactor was cooled and disassembled for material characterization. After the experiments with N_2 flow for 2 hours and 18 hours, alloy samples were collected from the upper, middle and lower parts along the solidified Li–Zn columns, and characterized by XPS. Their N 1s XPS signals were all below the detection limit (Fig. S6†), confirming that Li_3N floated up and dissolved into the molten salt on top of the alloy. To further quantify the nitrogen content, three pieces of solidified alloy (0.1165 g, 0.0998 g, and 0.1522 g) were sampled, and each was placed into 10 mL of 0.05 mol L^{-1} H_2SO_4 aqueous solution to dissolve any Li_3N. Based on the UV-Vis measurements of the solutions, the nitrogen weight fractions in those three solidified alloy samples were determined to be 0.039%, 0.051%, and 0.011%, respectively; these small values were consistent with the absence of N 1s XPS peaks in Fig. S6.† The result demonstrated the validity of using the molten LiCl–KCl to collect and quantify the amount of Li_3N fixed.

Fig. 3b shows the nitrogen weight fraction in the salt by analyzing five solidified samples from each experiment and then taking the mass-weighted average (see detailed data in Table S3†). In each experiment, the relatively homogeneous distribution of nitrogen in the solidified salt was consistent with the dissolution and ionization of Li_3N in the molten salt (reaction (3)). The tiny amount of nitrogen in the impurities of the commercial LiCl and KCl was subtracted (Fig. S7†).[65] The N weight fraction in the salt increased with the reaction time (Fig. 3b). Yet, the increase gradually slowed down, likely because the reaction of Li with N_2 reduced the Li molar content in the alloy (*e.g.*, from 70% to 66.81% for the 18-hour experiment). The Li activity declined exponentially with the decreasing content,[45] and accordingly the ability of the liquid alloy for N_2 fixation gradually became weaker. In addition, the Li content decrease shifts the alloy composition towards the liquidus line based on the Li–Zn phase diagram (Fig. S1a†) and might change the physicochemical properties (*e.g.*, viscosity and surface tension) of the liquid alloy. Besides, foaming and channel formation in the liquid alloy could also be possible. Their effects on N_2 fixation will be investigated in future studies.

To evaluate the temperature dependence of the N_2 fixation rate, we performed a series of experiments at different temperatures from 380 to 450 °C using the setup shown in Fig. 3a. Each experiment last for 2 hours. The nitrogen fixation rate by the 70 mol% Li–Zn liquid alloy was calculated by dividing the total amount of Li_3N in the salt above by the reaction time (Note S1 and Fig. S8†). Fig. 3c shows the Arrhenius plot of the natural logarithm of the N_2 fixation rate *vs.* $1/RT$, where R is the gas constant (8.31 J K^{-1} mol^{-1}). The value of the apparent activation energy (E_a) for N_2 fixation by the liquid Li–Zn was determined to be approximately 48.69 kJ mol^{-1}, equivalent to 0.51 eV. Such a low energy barrier was mainly attributed to the high activity of Li for N_2 activation and fixation,[35] as the overlap between the Zn d orbital and the Li s orbital was relatively small,[66] as will be discussed in section 3.1.3. To investigate the contribution of Zn to N_2 fixation and the subsequent NH_3 synthesis, we performed another experiment with a liquid catalytic system comprising pure Zn (height: 5 cm) and eutectic molten LiCl–KCl on the top (height: 5 cm) at 500 °C (Fig. S9†). The results suggest that the liquid Zn itself has negligible activity for N_2 fixation.

3.1.3. Understanding N_2 fixation by Li–Zn from AIMD simulations. To gain insights into N_2 fixation by the Li–Zn liquid alloy, we investigated this reaction by combining density functional theory (DFT)-based *ab initio* molecular dynamics (AIMD) simulations with the free energy sampling method. From the aspect of theoretical modeling, one important obstacle in understanding the reaction mechanism is the accurate description of the random nature and the complex and dynamic structure of the melts. The AIMD simulation is a straightforward method to treat the movement of liquid species at finite temperatures.[56,67] The computational details are provided in Note S7.†

To examine the reactivity of N_2 cleavage in liquid 70 mol% Li–Zn alloy, a randomly mixed $Li_{42}Zn_{18}$ model was built in a periodic cubic cell with the edge length = 11.2 Å. Then, a N_2 molecule was placed in the cell, and a pre-relax simulation was performed for 5 ps, allowing the liquid catalyst around the N_2 molecule to find the favorable arrangements. Fig. 3d shows the structure obtained, suggesting that the distributions of the Li and Zn atoms were not entirely random after the pre-relax simulation (Fig. S10a and b†). Further AIMD simulations were performed under the experimental condition of 400 °C. Fig. 3h shows the free energy change for N_2 cleavage to two $N^{\delta-}$ as a function of the N–N distance. The value of δ was calculated to be 3.3 ± 0.2 based on the Bader charge analysis.[68] The activation free energy (G_a) is defined as the energy difference between the transition state (TS) and the initial state (IS), and the reaction free energy (ΔG) is defined as the energy difference between the final state (FS) and the IS. The N_2 cleavage in the liquid Li–Zn alloy showed a G_a of 1.0 eV and ΔG of −0.5 eV, which are much lower than the cleavage in the gas phase.[69] The results suggest that the N_2 cleavage would be favorable in the liquid Li–Zn than in the gas. There is a discrepancy between the theoretical G_a and experimental values from the Arrhenius plot. The discrepancy may have two main origins: firstly, the slope of the Arrhenius plot is the activation enthalpy actually, rather than the activation free energy; and secondly, the dissolution of N_2 in the liquid alloy was not taken into account in the theoretical model. In spite of this, the main catalytic mechanisms can still be captured through theoretical simulations. The local environment near N_2 in the IS, TS and FS is illustrated in Fig. 3e–g, respectively. From these figures we found that, in each stage of N_2 cleavage, only Li atoms in the Li–Zn alloy interact with the N atoms, while Zn atoms rarely appear in the vicinity of the N atom. The results indicate that the N_2 cleavage in the Li–Zn liquid alloy is assisted by the Li atoms, and the Zn atoms mainly act as a

solvent for Li. Notably, Zn was added to the experimental system mainly based on the following considerations. First, the addition of Zn increases the density of the liquid alloy. Thus, the liquid alloy could stay beneath the molten salt (Fig. 1a and 3a), and the Li_3N formed by the reaction between N_2 and Li in the alloy could float to the molten salt. Second, adding Zn can reduce the activity of Li, decreasing the corrosiveness to the alumina reactor.

To investigate the impact of Zn addition on the Li activity in the 70 mol% Li–Zn liquid alloy, we conducted an analysis of the projected density of states (PDOS) in the $Li_{42}Zn_{18}$ model. The PDOS analysis (Fig. S10c and d†) indicates a reduced overlap of the d orbital of Zn and the s orbital of Li, consistent with previous findings,[66] despite the differences in their modeling system where the Li atoms were aggregated. These computational results demonstrate that in the Li–Zn system, the charge transfer from Zn to Li atoms is minimal, and as a result, the activity of Li is not significantly hindered for N_2 fixation.

We also examined the reactivity of N_2 cleavage in liquid pure Zn (Note S2, Fig. S10e and f†), liquid pure Li (Note S2, Fig. S10g and h†), and liquid 60 mol% Li–Sn alloy (Note S3

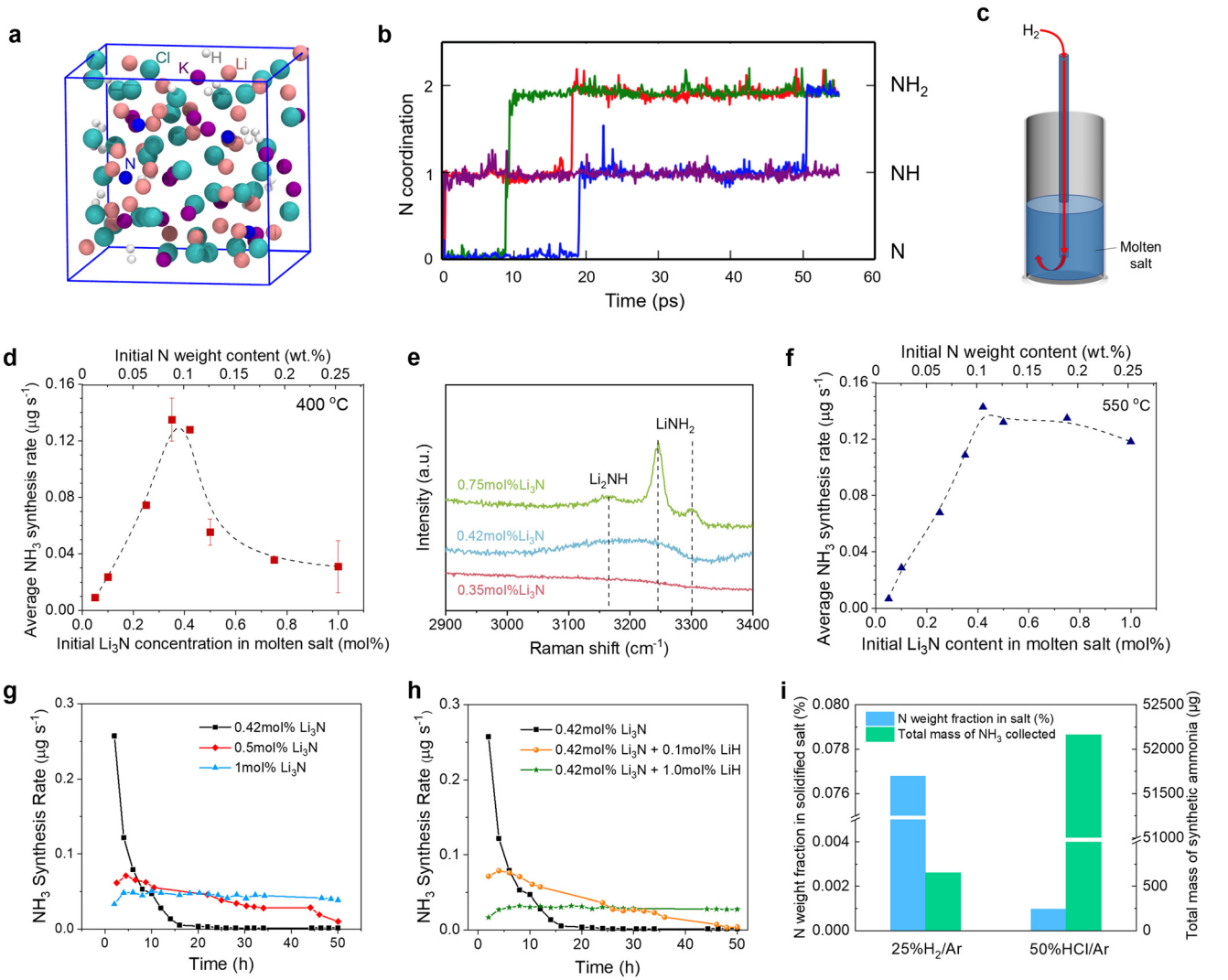

Fig. 4 The reaction of Li_3N with H_2 for NH_3 synthesis in the molten salt. (a) A snapshot of the model system of Li_3N hydrogenation reaction in the molten LiCl–KCl at the end of the AIMD simulation. Color code: pink, Li; purple, K; cyan, Cl; blue, N; white, H. (b) The trajectory of the coordination number of each of the four N atoms in the AIMD simulation. Different colors were used for these trajectories. (c) Schematic diagram of the experimental setup for bubbling H_2 (15 cm^3 min^{-1}) to the eutectic LiCl–KCl molten salt (height: 5 cm) containing Li_3N. The dependence of the average NH_3 synthesis rate on the Li_3N content in the molten salt in the experiments carried out for 8 hours at (d) 400 °C and (f) 550 °C. The dashed lines in (d) and (f) serve as guides for the eyes. (e) Raman spectra in the N–H stretching region of the solidified salt samples collected from the experiments that originally contained 0.35, 0.42, and 0.75 mol% Li_3N at 400 °C. The time dependence of the NH_3 synthesis rate measured for the 50-hour experiments of bubbling H_2 into (g) the eutectic LiCl–KCl molten salts containing varying amounts of Li_3N (0.42 mol%, 0.5 mol%, and 1.0 mol%) and (h) the eutectic LiCl–KCl molten salts containing 0.42 mol% Li_3N and varying amounts of LiH (0%, 0.1 mol%, and 1.0 mol%). (i) The N weight fractions in the solidified salts and the total amounts of NH_3 collected in the experiments of feeding 25% H_2/Ar or 50% HCl/Ar to the melts containing 0.5 mol% Li_3N at 500 °C.

and Fig. S11†) with AIMD simulations. A comparison of the results suggests that the N_2 cleavage in the pure liquid Zn is difficult due to the high activation energy of almost 4 eV. The liquid 70 mol% Li–Zn with a G_a of 1 eV is more reactive than the liquid 60 mol% Li–Sn with a G_a of 1.7 eV for N_2 activation. The N_2 cleavage in pure liquid Li shows a G_a of 0.8 eV, which is only 0.2 eV smaller than that in the 70 mol% Li–Zn. It can be inferred that the activity mainly originates from the high electron-donating ability of Li, and the 70 mol% Li–Zn liquid alloy still maintains the high activity of Li for N_2 fixation.

3.2. The reaction of Li_3N with H_2 for NH_3 synthesis in the molten salt

3.2.1. Reactivity of Li_3N with H_2 in the molten salt. In the liquid alloy–salt catalytic system, the Li_3N formed in the Li–Zn liquid alloy would float up and dissolve into Li^+ and N^{3-} in the molten salt. Previous studies have reported that the Li_3N dissolved in the molten salt promotes the spontaneous disproportionation of H_2, resulting in NH_3 synthesis in the experiments at 450 and 510 °C.[40,48] The hydrogenation of N^{3-} dissolved in the molten salt has faster kinetics and a smaller activation barrier compared with that in the solid-state Li_3N.[40,70,71] To investigate the reactivity of Li_3N in the molten LiCl–KCl with H_2, we carried out AIMD simulation by building a randomly mixed system composed of 4 Li_3N + 20 LiCl + 20 KCl in a periodic cubic cell of the edge length = 14.0 Å. Subsequently, 12 H_2 molecules were placed in the cell. Fig. 4a illustrates a snapshot of the system. To accelerate the reaction, the AIMD simulation was performed at an elevated temperature of 927 °C (1200 K). The basis for the use of elevated temperature is the assumption that the process shows Arrhenius behavior; *i.e.*, increasing temperature does not alter the pathway but only the rate.

From Fig. 4b, it is obvious that the two N^{3-} ions were readily hydrogenated to NH^{2-} within only hundreds of femtoseconds (fs), suggesting that the models composed of N^{3-} and H_2 were quite reactive. After 55 picoseconds (ps) of the AIMD simulation, the formation of three NH_2^- and one NH^{2-} was observed, as shown in Fig. 4a and b. No NH_3 was observed in the simulation, probably because the simulation time was still shorter than the experimental condition. The hydrogenation to NH_3 may need a much longer time which is beyond the computational capacities. Moreover, no dehydrogenation processes occurred in the simulations. Therefore, we predict that the hydrogenation of Li_3N in the molten salt is reactive under the experimental conditions, and occurs stepwise as described by reactions (4a)–(4c). It's also noted that, through simulation, we found that some nitrogen ions are bound to the surrounding Li ions, making it difficult for these nitrogen ions to come into contact and react with H_2. The results suggest that it's vital to separate the Li^+ and the nitrogen ions dissolved in the molten salt to accelerate NH_3 synthesis.

3.2.2. The effect of Li_3N concentration in the molten salt on NH_3 synthesis. Since the Li–Zn alloy has a strong ability for N_2 activation and fixation, a significant amount of Li_3N could be formed in the alloy and then dissolved as Li^+ and N^{3-} in the molten LiCl–KCl (Fig. 3b). The N^{3-} ions can react with the proton source such as H_2 to produce NH_3 (reaction (4)). Nevertheless, the excessive N^{3-} along with the chloride salts[72] might absorb the NH_3 produced and suppress its release (reaction (7)).[48,73] As inspired by Sabatier's principle in catalysis,[74] we hypothesize that the N^{3-} concentration in the molten salt should be neither too high nor too small, and the optimal NH_3 yield occurs when the N^{3-} concentration in the molten salt is of an intermediate value.

$$N^{3-} + NH_3 \rightarrow NH_2^- + NH^{2-} \quad (7)$$

To test the hypothesis, we performed experiments to investigate the effect of the Li_3N concentration on NH_3 synthesis at 400 °C in bubble column reactors (Fig. 4c). In each experiment, the LiCl–KCl eutectic molten salt (height: 5 cm) initially contained the desired amount of Li_3N varying from 0 to 1 mol%, and H_2 was bubbled into the molten salt at 15 cm^3 min^{-1} for 8 hours. The Li_3N used was synthesized by reacting pure Li tablets with N_2 at 100 °C (Note S4 and Fig. S12†). The Li_3N concentrations in the all the experiments were below its solubility limit in the salt.[46,47] Fig. 4d shows a typical volcano plot. The average NH_3 synthesis rate first increased and then decreased with the Li_3N concentration; *i.e.*, there was an optimum value for the Li_3N concentration in the molten salt for NH_3 synthesis. Such behavior was attributed to the aforementioned competing factors including NH_3 formation and absorption (reactions (4) and (7)). For a very low Li_3N concentration, the average NH_3 synthesis rate was limited by the availability of N^{3-} at the salt/bubble interface to react with H_2. As the Li_3N concentration increased, reaction (4) shifted to the right and favored NH_3 formation. Nevertheless, as the Li_3N concentration increased beyond approximately 0.4 mol%, the enhancement of NH_3 absorption (reaction (7)) exceeded the formation of NH_3 (reaction (4)). The NH_3 desorption started to become limiting, and therefore the average NH_3 synthesis rate gradually decreased at 400 °C. It's noted that the composition of 0.4 mol% Li_3N in the eutectic LiCl–KCl corresponded to 0.1 wt% nitrogen in the salt. The results suggested that the N^{3-} concentration can modulate the absorption strength of the molten salt, a key factor for NH_3 release. After cooling, the solidified salt samples were collected from the experiments originally with 0.35, 0.42, and 0.75 mol% Li_3N. To avoid the moisture, they were enclosed in sealed quartz cuvettes inside an Ar-filled glovebox before Raman spectroscopy analysis (Fig. 4e). Only the salt with the relatively high original amount of Li_3N (0.75 mol%) exhibited the characteristic peaks at 3245 and 3300 cm^{-1} for $LiNH_2$ and at 3165 cm^{-1} for β-Li_2NH,[75–78] consistent with the strong NH_3 absorption by the excessive Li_3N (reaction (7)).

Using the setup shown in Fig. 4c, we also investigated the relation between the average NH_3 synthesis rate and the Li_3N concentration at 550 °C, a much higher temperature than the target operation temperature in this work (400 °C). The average NH_3 synthesis rate *vs.* the Li_3N concentration curve obtained at 550 °C also exhibited a volcano-like plot (Fig. 4f); yet, the changing trend was not exactly the same as that at 400 °C. In the low Li_3N concentration regime (0–0.4 mol%), the NH_3 synthesis rate for both temperatures was close. However, in the high Li_3N concentration regime (0.4–1 mol%), the average NH_3 synthesis rate at 550 °C decreased only slightly due to the following reasons. Reaction (7) became less thermodynamically favorable as the temperature increased from 400 °C to 550 °C (Fig. S1b†). In addition, the increased temperature would increase the kinetics of reaction (4), although reaction (4) became slightly unfavorable. Overall, the temperature increase exhibited a promoting effect for NH_3 synthesis in the high Li_3N concentration regime.

The time dependence of the NH_3 synthesis rate was also investigated in 50-hour experiments with H_2 (15 cm^3 min^{-1}) bubbled into the eutectic LiCl–KCl of different Li_3N concentrations (0.42, 0.5, and 1.0 mol%) at 400 °C and ambient pressure (Fig. 4g). In the experiment with 0.42 mol% Li_3N, the NH_3 synthesis rate decreased rapidly over the first 10 hours but the decreasing trend gradually slowed down, because the consumption of Li_3N and the accumulation of LiH made reaction (4) more difficult to proceed.[40] In the experiment with the Li_3N concentration raised to 0.5 mol%, the NH_3 synthesis rate increased in the beginning, reached a peak value (0.071 μg s^{-1}) at approximately 4.5 hours, and then gradually decreased. A delayed emergence of the peak for the NH_3 synthesis rate was due to the absorption of NH_3 (reaction (7)), consistent with previous studies.[48,79]

When the Li_3N concentration in the molten salt was further increased to 1.0 mol%, the NH_3 synthesis rate initially increased during the first 4 hours and then remained at a relatively stable value (Fig. 4g), indicating a subtle balance between various reactions. First, the high Li_3N concentration not only favored NH_3 production (reaction (4)) but also led to a strong absorption of NH_3 (reaction (7)). In addition, based on reactions (4c) and (6), the accumulation of $LiNH_2$ would increase the thermodynamic driving force to promote NH_3 production (reaction (6) was validated as shown in Fig. S13†). Eventually, the reaction products in the molten salt might be transformed into Li_2NH, $LiNH_2$, and LiH. Similar to Li_3N, LiH can absorb NH_3 as expressed by reaction (8), which is invertible to reaction (4c),[80] although the thermodynamic driving force for NH_3 absorption by LiH was smaller than that by Li_3N (Fig. S1b†).

$$LiH + NH_3 \rightarrow LiNH_2 + H_2 \quad (8)$$

To reveal the role of LiH in the NH_3 synthesis, we performed another two experiments of bubbling H_2 (15 cm^3 min^{-1}) into LiCl–KCl melts containing 0.42 mol% Li_3N–0.1 mol% LiH and 0.42 mol% Li_3N–1 mol% LiH, respectively, at 400 °C. As shown in Fig. 4h, with the addition of more LiH, the changing trend of the curve was similar to that of increasing Li_3N concentration. The results suggested that LiH and Li_3N played similar roles in NH_3 absorption based on reactions (7) and (8). The flattened NH_3 synthesis rate *vs.* time curves in Fig. 4g and h were enabled jointly by Li_3N and LiH in the molten salt. The results also indicated that controlling the concentrations of Li_3N and LiH in the molten salt was vital for improving the NH_3 synthesis rate.

3.2.3. HCl as an alternative proton source to react with Li_3N in the molten salt. Based on the experimental results above, the reaction of H_2 with Li_3N in the molten salt led to the accumulation of relatively stable intermediate species (*e.g.*, NH^{2-}, NH_2^-, and H^-). Although the NH^{2-}/NH_2^- species could react with H_2 to produce NH_3 (reactions (4b) and (4c); Fig. S1†), these reactions were thermodynamically unfavorable (Fig. S1b†). Therefore, the relatively stable NH^{2-}/NH_2^- intermediates resulted in a significant amount of N-containing species remaining in the molten salt, instead of all converting to NH_3. In other words, the accumulation of the NH^{2-}/NH_2^- species in the molten salt corresponded to the limited NH_3 synthesis. Here, we investigated the use of hydrogen chloride (HCl) gas as an alternative proton source to react with Li_3N in the molten salt to produce NH_3, as expressed by reaction (9).[63] We performed two control experiments of feeding 25% H_2/Ar (20 cm^3 min^{-1}) and 50% HCl/Ar (20 cm^3 min^{-1}), respectively, into LiCl–KCl melts containing 0.5 mol% Li_3N for 1 hour at 500 °C. Afterwards, pure Ar (20 cm^3 min^{-1}) was bubbled to the melt for another 3 hours to purge NH_3 before cooling down the reactor in each experiment. NH_3 was collected throughout the 4 hours using the 0.05 mol L^{-1} aqueous H_2SO_4 solution. It's noted that dry 50% HCl/Ar (20 cm^3 min^{-1}) was made in the lab by passing a mixture of H_2 (5 cm^3 min^{-1}) and Ar (10 cm^3 min^{-1}) through a quartz tube containing anhydrous $NiCl_2$ at 700 °C in a horizontal furnace. Fig. 4i shows the nitrogen weight fractions in the solidified salts and the total amounts of ammonia collected in the H_2SO_4 solutions. A comparison of the results indicated that HCl was much more effective than H_2 in converting Li_3N to NH_3. In the reaction between H_2 and Li_3N in the molten salt, HCl might be introduced to the melt occasionally to control the nitrogen concentration and improve the NH_3 synthesis rate.

$$3HCl + Li_3N \rightarrow NH_3 + 3LiCl \quad (9)$$

In addition to NH_3, reaction (9) also produces LiCl which in principle can be electrolyzed to generate Li and Cl_2. Li can be used to fix N_2 and form Li_3N, while Cl_2 can react with H_2 to regenerate HCl, which would react with Li_3N to produce more NH_3 according to reaction (9). This closed-loop process for improving NH_3 synthesis is beyond the scope of the current study, and will be investigated in the future work.

3.3. The reaction of LiH with N_2 for NH_3 synthesis in the molten salt

LiH is a byproduct of the reaction between H_2 and Li_3N in the molten salt based on reaction (4). The accumulation of LiH in the molten salt has been identified to reduce the thermodynamic driving force for NH_3 synthesis.[40] The solid LiH is known to have a high thermodynamic stability due to the presence of a strong ionic bond, and its decomposition to Li and H_2 typically requires high temperatures above 700 °C.[81] To destabilize the LiH dissolved in the molten salt, previous work has proposed using a third element (*e.g.*, Sn) to alloy with Li upon LiH decomposition. This method of alloying lowered the energy barrier for LiH decomposition; however, LiH decomposition was still a thermodynamically unspontaneous reaction at the operation temperatures. The effectiveness of Li recovery from LiH decomposition with this method remains to be critically determined.

To evaluate the difficulty of LiH decomposition in the presence of the Li–Zn alloy (reaction (5)), we used AIMD to simulate the reverse reaction and investigate the reactivity of H_2 with the 70 mol% Li–Zn alloy. A randomly mixed $Li_{42}Zn_{18}$ system was built in a periodic cubic cell with the edge length = 11.2 Å, and a H_2 molecule was placed inside, as shown in Fig. 5a. The AIMD simulation was performed at 400 °C. Fig. 5b shows the free energy change for H_2 cleavage to two H^- as a function of the H–H distance. The G_a for H_2 cleavage in the liquid Li–Zn alloy was merely 0.1 eV, much smaller than that in the gas phase. On the other hand, the G_a for LiH decomposition to form H_2 and Li–Zn alloy was identified to be merely 1 eV, validating reaction (5). Nevertheless, the results verified that LiH decomposition was unspontaneous; even with the presence of the Li–Zn alloy, the energy barrier of its decomposition was still much greater than that of its reverse reaction.

Given the difficulty of LiH thermal decomposition, here we investigated the reaction of LiH in the molten salt with N_2. The eutectic LiCl–KCl mixture containing 3 mol% LiH was first heated to 400 °C in Ar, and then fed with N_2 (15 cm^3 min^{-1}) to the bottom of the molten salt (Fig. 5c). Fig. 5d shows that the NH_3 synthesis rate was relatively small over 30 hours at 400 °C, indicating that the reaction of LiH with N_2 contributed little to NH_3 synthesis. Nevertheless, the solidified salt contained approximately 0.05 wt% of nitrogen based on the UV-Vis characterization (Fig. S15†), almost three times greater than that in the commercial LiCl–KCl salt (Fig. S7†), indicating nitrogen fixation by LiH. Raman spectroscopy of the solidified salt shows characteristic peaks at 3170 cm^{-1} and 3230 cm^{-1} for Li_2NH (Fig. 5e),[77] indicating that the major product of the reaction between LiH and N_2

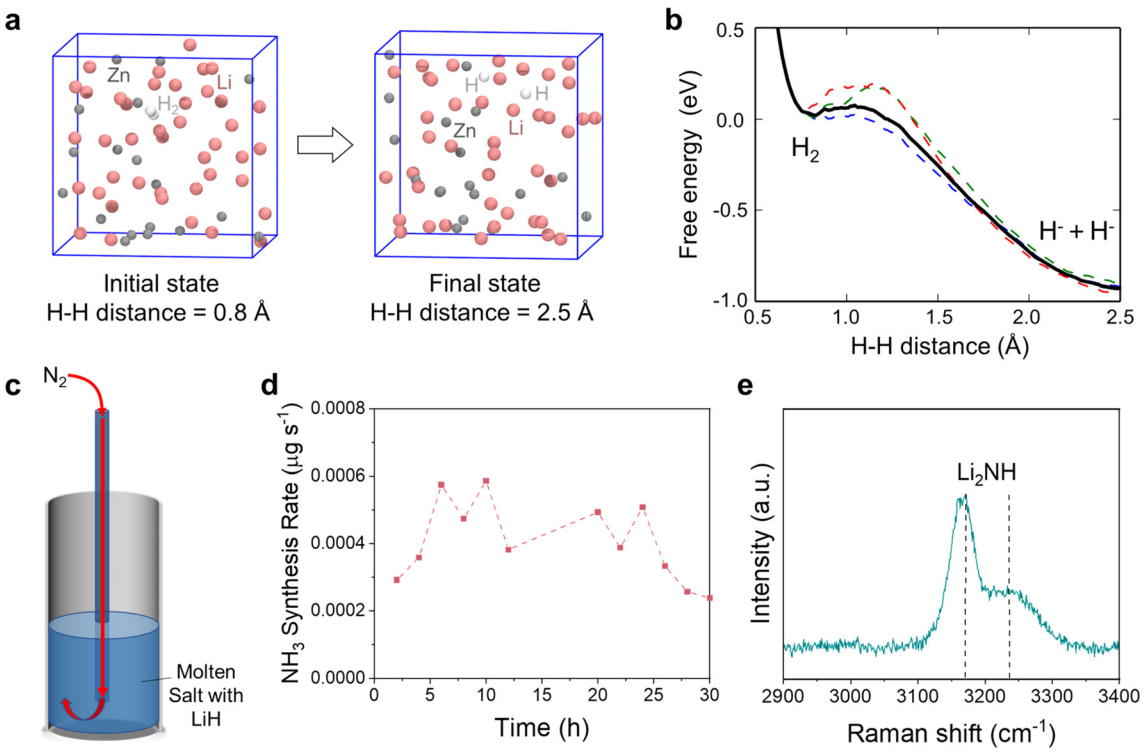

Fig. 5 (a) Snapshots of the initial state and the final state of the model system where the cubic box represents the periodic unit cell of the infinite bulk system. Color code: pink, Li; gray, Zn; white, H. (b) The free energy profile as a function of the H–H distance during the H_2 cleavage process, as denoted by the black bold line. The work profiles of 3 slow-growth trajectories are also shown, as denoted by the dashed lines in color. (c) Schematic diagram of the experimental setup for bubbling N_2 (5 cm^3 min^{-1}) to the eutectic LiCl–KCl molten salt (height: 5 cm) containing 3 mol% LiH. (d) The NH_3 synthesis rate measured for the experiment illustrated in (c) over 30 hours at 400 °C. (e) Raman spectrum of the solidified salt sample from the experiment showing characteristic peaks for Li_2NH.

was Li_2NH (reaction (10)). The degree of nitridation of LiH dissolved in the molten LiCl–KCl salt was calculated to be 13.18% at 400 °C (Note S5†). The dissolution of LiH in the molten salt enabled a gas–liquid reaction between LiH and N_2 in the bubbles. Unlike the gas–solid reaction between N_2 and solid LiH, the Li_2NH product dissolved into the molten salt without forming a blocking layer to hinder further reaction. In addition, Li_2NH may be further utilized by reacting with H_2 to form NH_3 (reactions (4b) and (4c)), but the resulting NH_3 synthesis rate was supposed to be limited as these reactions were thermodynamically unfavorable (Fig. S1b†). In principle, Li_2NH in the molten salt may also be converted to NH_3 by using HCl gas as an alternative and more effective proton source (reaction (11)), as discussed in section 3.2.3.

$$4LiH + N_2 \rightarrow 2Li_2NH + H_2 \quad (10)$$

$$Li_2NH + 2HCl \rightarrow 2LiCl + NH_3 \quad (11)$$

3.4. NH_3 synthesis in the liquid alloy–salt catalytic system

The combined experiments and simulations above have shown that the Li–Zn alloy is effective for fixing N_2, and the hydrogenation of Li_3N dissolved in the molten salt is reactive. We then investigated the effects of multiple variables on NH_3 synthesis from N_2 and H_2 in the molten catalytic system comprising the Li–Zn alloy and the LiCl–KCl salt.

3.4.1. The effect of temperature. We performed two experiments with the catalytic systems comprising 70 mol% Li–Zn alloy (height: 5 cm) and LiCl–KCl salt (height: 5 cm) at 400 °C and 500 °C, respectively. N_2 (5 cm^3 min^{-1}) and H_2 (15 cm^3 min^{-1}) were fed to the liquid alloy and molten salt, respectively (Fig. 1a). The NH_3 synthesis rates were measured over 18 hours at these temperatures; the data exhibited similar trends, starting with a gradual increase and then reaching steady values (Fig. 6a). Notably, in the first 4 hours, the NH_3 synthesis rate at 400 °C was almost zero, whereas the NH_3 synthesis rate at 500 °C was relatively large. The stable value of the NH_3 synthesis rate at 500 °C was also slightly greater than that at 400 °C, albeit with some fluctuations. This difference was attributed to the following factors. First, NH_3 synthesis from N_2 and H_2 is an exothermic and entropy-decreasing reaction. Although lower temperature was thermodynamically beneficial to NH_3 yield, this reaction was kinetically restricted due to the stable N≡N bonds and the short residence time of the bubbles in the alloy column (5 cm).[5] Increasing the temperature generally promoted the kinetics of nitrogen fixation. Second, the $\Delta G°$ of the reaction between Li_3N and NH_3 (reaction (7)) became less negative with the increase of temperature (Fig. S1b†), weakening the NH_3 absorption and increasing the NH_3 release. As shown in Table S4,† the N weight fraction in the solidified LiCl–KCl salt from the experiment at 500 °C was 0.783 wt%, still larger than that at 400 °C (0.559 wt%). The results indicated that, although the NH_3 absorption was weakened, the nitrogen fixation ability of Li was stronger at a higher temperature. Nevertheless, it should be noted that the steady values for NH_3 synthesis at 400 °C and 500 °C were relatively close, indicating it suitable to operate at relatively low temperatures, especially considering the development trend toward milder and greener conditions for NH_3 synthesis.

3.4.2. The effect of the feeding mode of N_2 and H_2. There were different ways of feeding N_2 (5 cm^3 min^{-1}) and H_2 (15 cm^3 min^{-1}) into the molten catalytic system comprising 70 mol% Li–Zn (height: 5 cm) and LiCl–KCl (height: 5 cm). In the first way of feeding N_2 and H_2 separately into the liquid alloy and the molten salt, the NH_3 synthesis rate gradually increased with time and stabilized at ~0.11 μmol g_{cat}^{-1} h^{-1} (equivalent to ~0.012 μg s^{-1}) (Fig. 6b). Meanwhile, in the second way of feeding the N_2 and H_2 mixture into the bottom of the liquid alloy, the NH_3 synthesis rate followed a similar trend and stabilized at ~0.15 μmol g_{cat}^{-1} h^{-1} (equivalent to

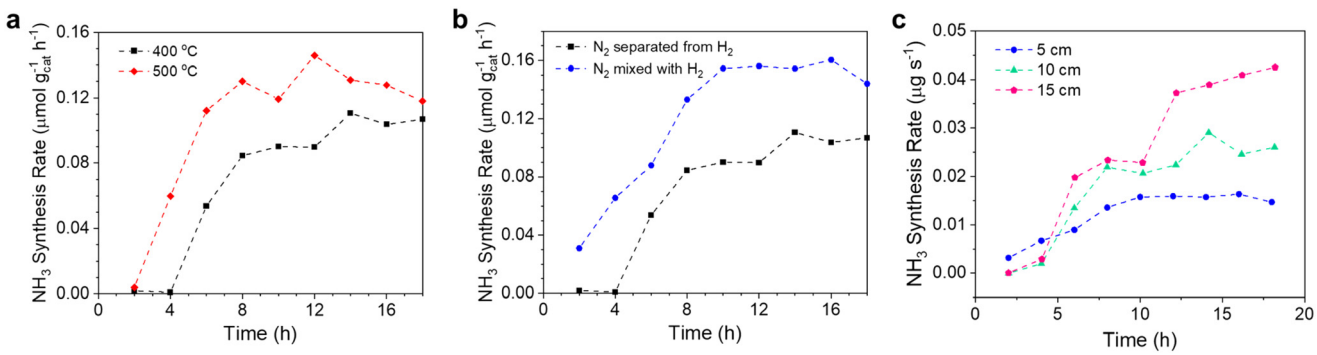

Fig. 6 (a) The NH_3 synthesis rate in liquid catalytic systems comprising Li–Zn alloy (height: 5 cm) and molten LiCl–KCl (height: 5 cm) at 400 and 500 °C. N_2 (5 cm^3 min^{-1}) and H_2 (15 cm^3 min^{-1}) were fed to the alloy and the salt, respectively. (b) The NH_3 synthesis rate in liquid catalytic systems comprising Li–Zn alloy (height: 5 cm) and molten LiCl–KCl (height: 5 cm) at 400 °C. In one experiment as denoted by black squares, N_2 (5 cm^3 min^{-1}) and H_2 (15 cm^3 min^{-1}) were fed to the alloy and salt, respectively. In the other experiment as denoted by the blue spheres, the mixture of N_2 (5 cm^3 min^{-1}) and H_2 (15 cm^3 min^{-1}) was fed to the liquid alloy. (c) The NH_3 synthesis rate in liquid catalytic systems comprising Li–Zn (5 cm) and LiCl–KCl of different heights (5, 10, and 15 cm). The mixture of N_2 (5 cm^3 min^{-1}) and H_2 (15 cm^3 min^{-1}) was directly introduced to the liquid alloy.

~0.016 μg s^{-1}) (Fig. 6b). The improvement in the NH_3 synthesis rate was enabled by changing the way of flowing N_2 and H_2 into the catalytic system. Such improvement was likely attributed to the following factors. First, in the case of mixing N_2 and H_2, the partial pressure of N_2 reacting with the 70 mol% Li–Zn alloy was lower, so the nitrogen fixation rate and the amount of Li_3N formed decreased, resulting in a weakened absorption of NH_3. The effect of N_2 partial pressure on the nitrogen fixation rate was further verified by performing control experiments (see more details in Note S6†). Second, when the mixture of N_2 and H_2 was passed into the bottom of the Li–Zn alloy, the reaction ($2Li + H_2 \rightarrow 2LiH$) also consumed a portion of Li, which competed with the nitrogen fixation and lowered the amount of Li_3N produced.[45] In the case of feeding the gas mixture, the N weight fraction in the solidified salt was indeed lower (0.407 wt%) (Table S4†). Third, H_2 can react with Li_3N the moment it was formed in the alloy when feeding the N_2–H_2 mixture, increasing the reaction time and enabling more reaction pathways for NH_3 synthesis. Therefore, the NH_3 synthesis rate was greater in the case of feeding the mixture of N_2 and H_2 than feeding them separately. Feeding the mixture of N_2 and H_2 reduces the complexity of the setup, and brings the system closer to industrial reaction conditions where the unreacted N_2 and H_2 mixture can be recycled back into the reactor after ammonia separation.[10]

3.4.3. The effect of the molten salt height. The effect of the height of the eutectic LiCl–KCl molten salt on the NH_3 synthesis rate was also investigated. We performed three experiments on the molten catalytic systems comprising 70 mol% Li–Zn of a fixed height of 5 cm and LiCl–KCl of three different heights (5, 10, and 15 cm) at 400 °C. The mixture of N_2 (5 cm^3 min^{-1}) and H_2 (15 cm^3 min^{-1}) was fed into the bottom of the liquid alloy. Fig. 6c shows the NH_3 synthesis rate monitored over 18 hours in these experiments, which exhibited similar trends, starting with a gradual increase in the first 10 hours and then reaching relatively steady values. As the height of the molten salt column increased from 5 cm, 10 cm, to 15 cm, the NH_3 synthesis rate at the 18th hour increased from 0.015 μg s^{-1} (0.121 μmol g_{cat}^{-1} h^{-1}), 0.026 μg s^{-1} (0.132 μmol g_{cat}^{-1} h^{-1}), to 0.043 μg s^{-1} (0.137 μmol g_{cat}^{-1} h^{-1}), respectively. After cooling to room temperature, the solidified salt samples were characterized to measure the nitrogen content. The nitrogen weight fraction decreased from 0.407 wt%, 0.304 wt%, to 0.276 wt%, with the increase of the salt column height (Table S4†). The decrease of the Li_3N concentration in this range weakened the NH_3 absorption and thereby increased the NH_3 synthesis rate, based on the volcano plot (Fig. 4d). The results indicate the feasibility of raising the height of molten LiCl–KCl salt for improving the NH_3 synthesis rate.

3.5. Summary of major reactions in the liquid catalytic system and the outlook

Improving the understanding of the molten catalytic system provides a guideline for designing better molten catalytic systems. The lithium-based loop presented in the previous work is over-simplified.[40] Based on the afore-mentioned experimental and simulation results, here we have proposed a more complete picture of the major reactions taking place in the molten catalytic system for NH_3 synthesis from N_2 and H_2, as illustrated in Fig. 7. The ammonia synthesis process involves multiple reaction steps especially in the molten salt.

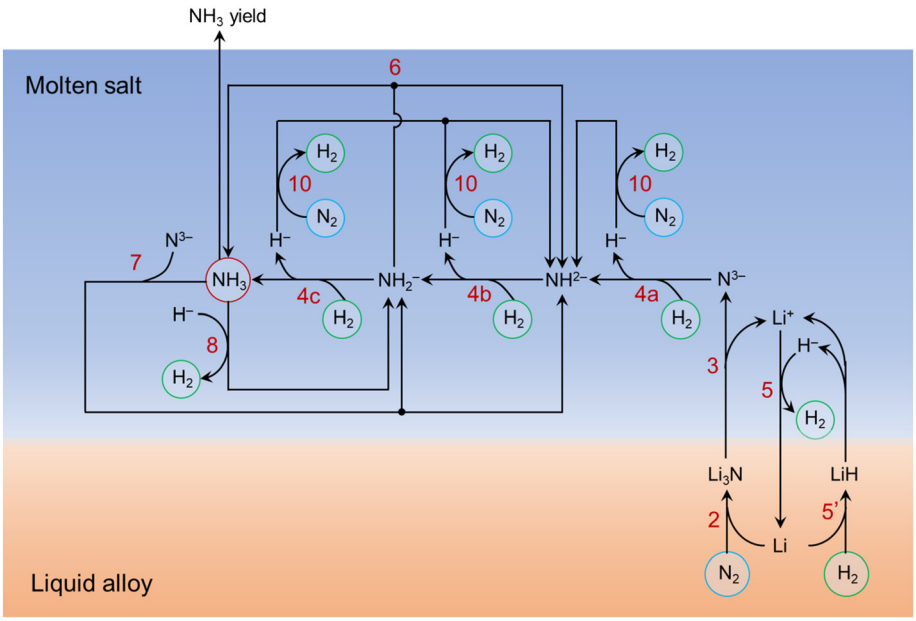

Fig. 7 A holistic illustration of the major reactions taking place in the molten catalytic system comprising Li–Zn alloy and LiCl–KCl salt. The gaseous molecules (N_2, H_2, NH_3) are circled to increase clarity. The numbers in red refer to the reactions listed in the main text. The effect of HCl is not considered here. Reaction (5′) is the reverse of reaction (5).

It has taken into account the stepwise reactions of N^{3-} hydrogenation (reactions (4a)–(4c)), the absorption of NH_3 by N^{3-} (reaction (7)) and H^- (reaction (8)), and N_2 fixation by H^- (reaction (10)). Reactions (6), (7), (8), and (10) lead to the accumulation of the relatively stable intermediate species (*i.e.*, NH^{2-}, NH_2^-) in the molten salt, corresponding to the limited NH_3 yield, as discussed in section 3.2.3.

To evaluate the catalytic performance of the molten catalytic system for ammonia synthesis from N_2 and H_2, we have compared the activity levels of the molten catalytic systems studied in this work with several relevant catalysts reported in the literature, as summarized in Table S5.† The highest activity level obtained was 0.137 μmol g_{cat}^{-1} h^{-1} in the molten catalytic system comprising 70 mol% Li–Zn (5 cm) and eutectic LiCl–KCl (15 cm) at 400 °C and 1 bar. This value was greater than that obtained in pure liquid sodium[29] but smaller than those of solid catalysts such as the Zn/LiH system,[59] La–TM–Si systems (TM═Co, Fe, Mn),[28] and Cs-promoted Ru/MgO.[82] Overall, the molten catalytic system has a significant ammonia yield rate but a low calculated activity level. The reason is actually clear. The molten catalytic system uses a heavy bubble column (21.55–39.15 g) with large-size bubbles at a limited flow rate (5–20 cm^3 min^{-1}), and the effective gas/liquid interfacial areas for nitrogen fixation and ammonia synthesis are small; in comparison, the solid catalysts reported in the literature[28,59,82] use much less material (0.03–0.1 g) with large surface areas and high gas flows.

Apparently, there are opportunities for improving the molten catalytic system for ammonia synthesis significantly. For example, the material selection for the liquid alloy and molten salt is not restricted to Li–Zn and LiCl–KCl. It is necessary to investigate other reactive alloys and ionic salts. It is also critical to advance the understanding of the high atomic mobility and the complex atomic structure in the melts of various compositions with *in situ* characterization techniques[83] and artificial intelligence methods,[84] which might considerably improve the catalytic performance of the system. The dynamic interface between the alloy and the salt is also of great interest. In addition, it will be necessary to carry out scale-up studies and develop pressurized reactors that allow the generation of a significant amount of very tiny gas bubbles to increase the area of the gas/liquid reaction interface. Besides, as indicated by Fig. 4i, the introduction of a suitable amount of HCl into the molten salt can improve the ammonia synthesis rate significantly due to rapid reactions of HCl with N^{3-}, NH^{2-}, and NH_2^-. HCl readily disturbs the accumulation of the relatively stable NH^{2-} and NH_2^- in the molten salt. Moreover, the liquid alloy–salt catalytic system can incorporate electrolysis to facilitate the ammonia synthesis and remove the oxide impurities if formed by the reaction between the reactive metal and any water or oxygen present in the feeding gas. These exciting research opportunities are worthy of thorough investigations in the future work.

4. Conclusions

The liquid alloy–salt catalytic system is an integrated, synergistic, and multi-phase (*i.e.*, liquid alloy, molten salt, gas bubbles) system that offers unique chemistry and reaction pathways for ammonia synthesis under relatively mild conditions. Through combined experiments and simulations, we have studied the mechanism of nitrogen fixation and ammonia synthesis in the catalytic system comprising liquid Li–Zn and molten LiCl–KCl. The 70 mol% Li–Zn liquid alloy is effective for N_2 dissociation and fixation, and Li is identified to be the reactive species. Li_3N floats from the self-cleaning liquid alloy to the highly ionic molten salt, circumventing the scaling relation exerted on Li. When feeding H_2 to the molten salt, the relationship between the Li_3N concentration in the molten salt and the NH_3 synthesis rate exhibits a volcano plot. In the liquid catalytic system, Li_3N is first formed in the alloy without LiH. The NH_3 generated from Li_3N and H_2 in the molten salt might be absorbed by the excessive Li_3N, limiting the NH_3 synthesis rate. As the reactions proceeds, LiH accumulates and absorbs NH_3 as well. These findings provide guidelines for the optimization of the experiments. Different strategies have been investigated for improving the NH_3 synthesis rate, including (i) feeding HCl to the salt, (ii) changing the temperature, (iii) flowing the mixture of N_2 and H_2 to the alloy, and (iv) increasing the height of the molten salt column. In summary, this work has demonstrated the effectiveness of the catalytic system based on liquid Li–Zn and molten LiCl–KCl for NH_3 synthesis at relatively low temperatures (400–500 °C) and ambient pressure, and will motivate further research and development on decentralized ammonia synthesis with complex melts.

Author contributions

X. G. conceived the study and supervised the project. X. M., Z. T., and B. X. performed the experiments, characterized the materials, and analyzed the data under X. G.'s guidance. J. L. and B. Y. designed and performed the AIMD simulations, and analyzed the computational results. P. Y. performed the STEM and EELS experiments and analyzed the results under K. C.'s guidance. X. W. assisted in the material characterization and the technical discussion. X. M., J. L., Z. T., B. X., B. Y., and X. G. wrote the manuscript with feedback from all authors.

Conflicts of interest

The following may be considered as potential conflict of interest: X. G., Z. T., and X. M. have patents (CN112266002A, CN112250088A) issued to ShanghaiTech University.

Acknowledgements

This material is based on the work supported by ShanghaiTech University. Part of the characterization

experiments was performed at the Analytical Instrumentation Center (SPST-AIC10112914) and the Center for High-resolution Electron Microscopy (ChEM, EM02161943) at ShanghaiTech University. The authors thank Ms. Jiayin Zhou for the kind help with the SEM, EDS, and Raman characterization, and Mr. Xu Zhang for generously sharing experiences in the HCl generation experiments.

References

1 D. R. MacFarlane, P. V. Cherepanov, J. Choi, B. H. R. Suryanto, R. Y. Hodgetts, J. M. Bakker, F. M. Ferrero Vallana and A. N. Simonov, *Joule*, 2020, **4**, 1186–1205.
2 N. Lazouski, Z. J. Schiffer, K. Williams and K. Manthiram, *Joule*, 2019, **3**, 1127–1139.
3 C. Smith and L. Torrente-Murciano, *Chem Catal.*, 2021, **1**, 1163–1172.
4 S. F. Yin, B. Q. Xu, X. P. Zhou and C. T. Au, *Appl. Catal., A*, 2004, **277**, 1–9.
5 Q. Wang, J. Guo and P. Chen, *J. Energy Chem.*, 2019, **36**, 25–36.
6 H. Liu, *Chin. J. Catal.*, 2014, **35**, 1619–1640.
7 A. Buttler and H. Spliethoff, *Renewable Sustainable Energy Rev.*, 2018, **82**, 2440–2454.
8 C. Zhou, J. Ni, H. Chen and X. Guan, *Sustainable Energy Fuels*, 2021, **5**, 4355–4367.
9 J. W. Erisman, M. A. Sutton, J. Galloway, Z. Klimont and W. Winiwarter, *Nat. Geosci.*, 2008, **1**, 636–639.
10 C. Smith, A. K. Hill and L. Torrente-Murciano, *Energy Environ. Sci.*, 2020, **13**, 331–344.
11 United Nations Sustainable Development Goals, **https://sdgs.un.org/goals**, (accessed 5/29/2023).
12 M. Kitano, Y. Inoue, Y. Yamazaki, F. Hayashi, S. Kanbara, S. Matsuishi, T. Yokoyama, S.-W. Kim, M. Hara and H. Hosono, *Nat. Chem.*, 2012, **4**, 934–940.
13 M. Kitano, S. Kanbara, Y. Inoue, N. Kuganathan, P. V. Sushko, T. Yokoyama, M. Hara and H. Hosono, *Nat. Commun.*, 2015, **6**, 6731.
14 M. Kitano, Y. Inoue, H. Ishikawa, K. Yamagata, T. Nakao, T. Tada, S. Matsuishi, T. Yokoyama, M. Hara and H. Hosono, *Chem. Sci.*, 2016, **7**, 4036–4043.
15 R. Kojima and K.-I. Aika, *Chem. Lett.*, 2000, **29**, 514–515.
16 P. Wang, F. Chang, W. Gao, J. Guo, G. Wu, T. He and P. Chen, *Nat. Chem.*, 2017, **9**, 64–70.
17 P. Mehta, P. Barboun, F. A. Herrera, J. Kim, P. Rumbach, D. B. Go, J. C. Hicks and W. F. Schneider, *Nat. Catal.*, 2018, **1**, 269–275.
18 T. Wang and F. Abild-Pedersen, *Proc. Natl. Acad. Sci. U. S. A.*, 2021, **118**, e2106527118.
19 X. Peng, H. X. Liu, Y. Zhang, Z. Q. Huang, L. Yang, Y. Jiang, X. Wang, L. Zheng, C. Chang, C. T. Au, L. Jiang and J. Li, *Chem. Sci.*, 2021, **12**, 7125–7137.
20 A. Vojvodic and J. K. Nørskov, *Natl. Sci. Rev.*, 2015, **2**, 140–143.
21 C. Mao, J. Wang, Y. Zou, G. Qi, J. Y. Yang Loh, T. Zhang, M. Xia, J. Xu, F. Deng, M. Ghoussoub, N. P. Kherani, L. Wang, H. Shang, M. Li, J. Li, X. Liu, Z. Ai, G. A. Ozin, J. Zhao and L. Zhang, *J. Am. Chem. Soc.*, 2020, **142**, 17403–17412.
22 Y. Gong, H. Li, C. Li, X. Yang, J. Wang and H. Hosono, *Chem. Mater.*, 2022, **34**, 1677–1685.
23 Z. Wang, Y. Gong, M. L. Evans, Y. Yan, S. Wang, N. Miao, R. Zheng, G.-M. Rignanese and J. Wang, *J. Am. Chem. Soc.*, 2023, **145**, 26412–26424.
24 S. Feng, Y. Yao, J.-C. Charlier, G.-M. Rignanese and J. Wang, *Chem. Mater.*, 2023, **35**, 9019–9028.
25 Y. Gong, J. Wu, M. Kitano, J. Wang, T.-N. Ye, J. Li, Y. Kobayashi, K. Kishida, H. Abe, Y. Niwa, H. Yang, T. Tada and H. Hosono, *Nat. Catal.*, 2018, **1**, 178–185.
26 Y. Gong, H. Li, J. Wu, X. Song, X. Yang, X. Bao, X. Han, M. Kitano, J. Wang and H. Hosono, *J. Am. Chem. Soc.*, 2022, **144**, 8683–8692.
27 Y. Gong, H. Li, C. Li, X. Bao, H. Hosono and J. Wang, *J. Adv. Ceram.*, 2022, **11**, 1499–1529.
28 H. Li, Y. Gong, H. Yang, X. Yang, K. Li, J. Wang and H. Hosono, *ChemSusChem*, 2023, **16**, e202301016.
29 F. Kawamura and T. Taniguchi, *Sci. Rep.*, 2017, **7**, 11578.
30 F. Kawamura, M. Morishita, K. Omae, M. Yoshimura, Y. Mori and T. Sasaki, *J. Mater. Sci.: Mater. Electron.*, 2005, **16**, 29–34.
31 D. Roy, A. Navarro-Vazquez and P. V. R. Schleyer, *J. Am. Chem. Soc.*, 2009, **131**, 13045–13053.
32 J. M. McEnaney, A. R. Singh, J. A. Schwalbe, J. Kibsgaard, J. C. Lin, M. Cargnello, T. F. Jaramillo and J. K. Nørskov, *Energy Environ. Sci.*, 2017, **10**, 1621–1630.
33 Z. Tang and X. Guan, *J. Sustain. Metall.*, 2021, **7**, 203–214.
34 O. Takeda, M. Li, T. Toma, K. Sugiyama, M. Hoshi and Y. Sato, *J. Electrochem. Soc.*, 2014, **161**, D820–D823.
35 S. Yamaguchi, T. Ichikawa, Y. Wang, Y. Nakagawa, S. Isobe, Y. Kojima and H. Miyaoka, *ACS Omega*, 2017, **2**, 1081–1088.
36 K. Shinzato, K. Tagawa, K. Tsunematsu, H. Gi, P. K. Singh, T. Ichikawa and H. Miyaoka, *ACS Appl. Energy Mater.*, 2022, **5**, 4765–4773.
37 T. Yamaguchi, K. Shinzato, K. Yamamoto, Y. Wang, Y. Nakagawa, S. Isobe, T. Ichikawa, H. Miyaoka and T. Ichikawa, *Int. J. Hydrogen Energy*, 2020, **45**, 6806–6812.
38 R. Michalsky, A. M. Avram, B. A. Peterson, P. H. Pfromm and A. A. Peterson, *Chem. Sci.*, 2015, **6**, 3965–3974.
39 K. Tagawa, H. Gi, K. Shinzato, H. Miyaoka and T. Ichikawa, *J. Phys. Chem. C*, 2022, **126**, 2403–2409.
40 Z. Tang, X. Meng, Y. Shi and X. Guan, *ChemSusChem*, 2021, **14**, 4697–4707.
41 K. Wang, K. Jiang, B. Chung, T. Ouchi, P. J. Burke, D. A. Boysen, D. J. Bradwell, H. Kim, U. Muecke and D. R. Sadoway, *Nature*, 2014, **514**, 348–350.
42 Y. Hu, G. Z. Chen, L. Zhuang, Z. Wang and X. Jin, *Cell Rep. Phys. Sci.*, 2021, **2**, 100425.
43 Z. J. Schiffer, A. M. Limaye and K. Manthiram, *Joule*, 2021, **5**, 135–148.
44 H. Okamoto, *J. Phase Equilib. Diffus.*, 2012, **33**, 345.
45 Z. Moser, F. Sommer, J. J. Lee and B. Predel, *Thermochim. Acta*, 1989, **142**, 117–125.

46 T. Goto, T. Iwaki and Y. Ito, *Electrochim. Acta*, 2005, **50**, 1283–1288.
47 T. Goto, K. Toyoura, H. Tsujimura and Y. Ito, *Mater. Sci. Eng., A*, 2004, **380**, 41–45.
48 I. J. McPherson, T. Sudmeier, J. P. Fellowes, I. Wilkinson, T. Hughes and S. C. E. Tsang, *Angew. Chem., Int. Ed.*, 2019, **58**, 17433–17441.
49 A. Jain, H. Miyaoka and T. Ichikawa, *Int. J. Hydrogen Energy*, 2016, **41**, 5969–5978.
50 Y. Wang, Y. Zhang and C. Wolverton, *Phys. Rev. B: Condens. Matter Mater. Phys.*, 2013, **88**, 024119.
51 X. Gu, J. Dong and C. Lai, *Eng. Rep.*, 2020, **3**, e12339.
52 T. R. Hogness, *J. Am. Chem. Soc.*, 1921, **43**, 1621–1628.
53 H. W. Davison, NASA Technical Note D-4650, 1968.
54 H. Ito, Y. Hasegawa and Y. Ito, *J. Chem. Eng. Data*, 2001, **46**, 1203–1205.
55 NIST X-ray Photoelectron Spectroscopy Database, NIST Standard Reference Database Number 20, National Institute of Standards and Technology, Gaithersburg MD, 20899 (2000), DOI: DOI: **10.18434/T4T88K**, (retrieved on 2023/5/29).
56 Q. Yang, J. Liu, C. Zhou, J. Ni, E. I. Vovk, Y. Yang, B. Yang and X. Guan, *Mater. Today Chem.*, 2022, **25**, 100949.
57 Q. Yang, C. Zhou, J. Ni and X. Guan, *Sustainable Energy Fuels*, 2020, **4**, 2768–2774.
58 Y. Sun, Y. Li, J. Sun, Y. Li, A. Pei and Y. Cui, *Energy Storage Mater.*, 2017, **6**, 119–124.
59 R. Wang, W. Gao, S. Feng, Y. Guan, Q. Wang, J. Guo and P. Chen, *ChemSusChem*, 2023, **16**, e202300813.
60 M. S. Kim, Z. Zhang, J. Wang, S. T. Oyakhire, S. C. Kim, Z. Yu, Y. Chen, D. T. Boyle, Y. Ye, Z. Huang, W. Zhang, R. Xu, P. Sayavong, S. F. Bent, J. Qin, Z. Bao and Y. Cui, *ACS Nano*, 2023, **17**, 3168–3180.
61 G. O. Hartley, L. Jin, B. J. Bergner, D. S. Jolly, G. J. Rees, S. Zekoll, Z. Ning, A. T. R. Pateman, C. Holc, P. Adamson and P. G. Bruce, *Chem. Mater.*, 2019, **31**, 9993–10001.
62 Y. Kojima, T. Ichikawa and H. Fujii, in *Encyclopedia of Electrochemical Power Sources*, ed. J. Garche, Elsevier, Amsterdam, 2009, pp. 473–483.
63 S. Suzuki, T. Shodai and J. Yamaki, *J. Phys. Chem. Solids*, 1998, **59**, 331–336.
64 F. Wang, S. W. Kim, L. Wu, D. Su, Y. Zhu and J. Graetz, *Microsc. Microanal.*, 2013, **19**, 1490–1491.
65 Y. Chen, H. Liu, N. Ha, S. Licht, S. Gu and W. Li, *Nat. Catal.*, 2020, **3**, 1055–1061.
66 Z. Zhang, Y. Zhao, B. Sun, J. Xu, Q. Jin, H. Lu, N. Lyu, Z.-M. Dang and Y. Jin, *ACS Appl. Mater. Interfaces*, 2022, **14**, 19419–19425.
67 C. Ruffman, K. G. Steenbergen, A. L. Garden and N. Gaston, *Chem. Sci.*, 2024, **15**, 185–194.
68 E. Sanville, S. D. Kenny, R. Smith and G. Henkelman, *J. Comput. Chem.*, 2007, **28**, 899–908.
69 D. C. Frost, C. A. McDowell and C. E. H. Bawn, *Proc. Math. Phys. Eng. Sci.*, 1956, **236**, 278–284.
70 H. M. Jin, J. Z. Luo and P. Wu, *Appl. Phys. Lett.*, 2007, **90**, 084101.
71 T. Murakami, T. Nishikiori, T. Nohira and Y. Ito, *J. Electrochem. Soc.*, 2005, **152**, D75.
72 T. Zhang, H. Miyaoka, H. Miyaoka, T. Ichikawa and Y. Kojima, *ACS Appl. Energy Mater.*, 2018, **1**, 232–242.
73 N. Serizawa, H. Miyashiro, K. Takei, T. Ikezumi, T. Nishikiori and Y. Ito, *J. Electrochem. Soc.*, 2012, **159**, E87.
74 M. Che, *Catal. Today*, 2013, **218–219**, 162–171.
75 Z. Li, J. Zhang, S. Wang, L. Jiang, M. Latroche, J. Du and F. Cuevas, *Phys. Chem. Chem. Phys.*, 2015, **17**, 21927–21934.
76 Y. Kojima and Y. Kawai, *J. Alloys Compd.*, 2005, **395**, 236–239.
77 B. Paik and A. Wolczyk, *J. Phys. Chem. C*, 2019, **123**, 1619–1625.
78 N. Serizawa, K. Takei, T. Nishikiori, Y. Katayama and Y. Ito, *Electrochemistry*, 2018, **86**, 88–91.
79 N. Serizawa, H. Miyashiro, K. Takei, T. Ikezumi, T. Nishikiori and Y. Ito, *J. Electrochem. Soc.*, 2012, **159**, E87–E91.
80 H. Miyaoka, H. Fujii, H. Yamamoto, S. Hino, H. Nakanishi, T. Ichikawa and Y. Kojima, *Int. J. Hydrogen Energy*, 2012, **37**, 16025–16030.
81 L. Wang, M. Z. Quadir and K.-F. Aguey-Zinsou, *Int. J. Hydrogen Energy*, 2016, **41**, 18088–18094.
82 Q. Wang, J. Pan, J. Guo, H. A. Hansen, H. Xie, L. Jiang, L. Hua, H. Li, Y. Guan, P. Wang, W. Gao, L. Liu, H. Cao, Z. Xiong, T. Vegge and P. Chen, *Nat. Catal.*, 2021, **4**, 959–967.
83 L. Chen, Z. Song, S. Zhang, C.-K. Chang, Y.-C. Chuang, X. Peng, C. Dun, J. J. Urban, J. Guo, J.-L. Chen, D. Prendergast, M. Salmeron, G. A. Somorjai and J. Su, *Science*, 2023, **381**, 857–861.
84 S. S. Fatima, K. Zuraiqi, A. Zavabeti, V. Krishnamurthi, K. Kalantar-Zadeh, K. Chiang and T. Daeneke, *Nat. Catal.*, 2023, **6**, 1131–1139.

